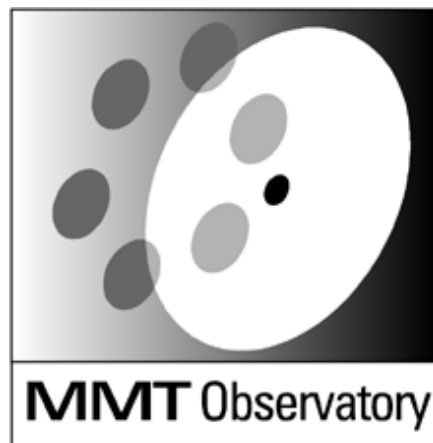# MMTO Technical Memorandum #10-1

Smithsonian Institution &
The University of Arizona®

Calibration and Correction of Amplifier Induced Artifacts in an Interleaved InSb Infrared Array

M. A. Kenworthy and P. M. Hinz

April 2010

Calibration and Correction of Amplifier Induced Artifacts in an Interleaved InSb Infrared Array

Matthew A. Kenworthy[1] and Philip M. Hinz

Steward Observatory, 933 North Cherry Avenue, Tucson, AZ 85721,

`kenworthy@strw.leidenuniv.nl`

USA

ABSTRACT

We present a method for the internal calibration of infrared array images where multiple amplifiers operate on interleaved columns, such as InSb arrays. A flux correction is estimated using a slope illumination across the detector, and a resultant lookup table is calculated for rapid conversion from raw detector counts to corrected image counts. The corrected images have all systematic column effects removed, enhancing sensitivity of contrast limited observations utilising point spread function modeling and subtraction.

Subject headings: instrumentation: techniques, infrared arrays

1. Introduction

Our motivation for this work is high contrast imaging in the thermal infrared, where we are searching for faint companions near bright stars. With direct imaging, there is diffracted starlight that rises above the sky background from 2 to 10 diffraction widths from the central Airy disk. Angular Differential Imaging and coronagraphic optics are employed to minimise the effects of the scattered light, but to do so we require images with high dynamic range that are free of detector based artifacts.

The Clio camera (Freed et al. 2004; Hinz et al. 2007) is designed for use on the MMTO 6.5m telescope in southern Arizona, to be used in conjunction with the adaptive secodnary

---

[1]Leiden Observatory, P.O. Box 9513, Niels Bohrweg 2, 2300 RA Leiden, The Netherlands

AO system. The low thermal emission with the simple optical path leads to a thermally clean optical imaging system. The Clio camera uses an Indigo Systems Indium Antimonide (InSb) 256x320 array bump-bonded onto an ISO9809 array (ROIC), chosen for the large well-depth and rapid readout. The detector is run with San Diego State University Generation II electronics with a modified timing board and DSP code for fast clocking of the array. The pixel clock is set at 200 kHz, and pixels are transmitted at each transition edge giving a pixel rate of 400 kHz. The high well depth of 3 million electrons and relatively low read noise of $350e^-$ at 77K (Sivanandam et al. 2006) make it appropriate for rapid readout thermal imaging.

Four separate amplifiers read out the array to increase the total readout speed. The four amplifiers (hereafter labelled A,B,C,D) read out the columns of the array in an interleaved order repeated across the array: ABCDABCDABCD..., so the final image can be thought of as four separate images interleaved sequentially on a per column basis. Previous measurements show that the gain of the A to D converter is about $85\text{-}90e^-$/DN (Sivanandam et al. 2006). An A to D converter takes the four amplifier voltages and converts them into a 16-bit unsigned number, with a data number (DN) in the range from 0 to 65535. The voltage levels in the converter are set such that the zero integration time has a count level of approximately 11000 DN. The well depth of the array is around 50000 DN, giving an approximate dynamic range of 39000 DN. The dark current of the array is measured to be approximately 2400 DN per second, resulting in saturation of the array in about 10 seconds. Observations are dominated by the sky background at thermal infrared wavlengths, and so the exposure time is set so that the typical observation has a sky background flux of 40000 DN, leaving a further range of 10000 DN before the full well level is reached. For L band, this is typically 2 to 4 seconds, and at M band, this is around 150-300 msec.

All four amplifiers are nominally identical, but differences in the tolerances of the discrete electronics in the amplifier result in gain curves that differ by a few percent with large systematic residuals.

2. Thermal Infrared Observations

The most common observing mode used in thermal imaging is beamswitching. The science target is placed on one side of the array (Beam A) and a frame is obtained. The science object is moved either to the other side of the array, or moved off the detector entirely to form Beam B. The sky background flux dominates over the flux from the science object, and so the subtraction of Beam B from Beam A ideally results in a complete subtraction of the sky background flux, the dark current from the detector, and the bias level of the array

as set by the A to D converter in the readout electronics.

In practice, there is a time varying component to the sky background flux which (to a good approximation) is a constant value across the $12'' \times 15''$ field of view, and so the beam subtraction results in a mean non-zero value for the sky background. The result is in Figure 1 (a). A periodic pattern amongst the columns is visible in the sky background regions of the image - this is due to the different responses for each of the four amplifiers.

2.1. Sky Background Limited Observations

For sky background limited observations, where the region around the science target is dominated by a smooth sky background. The most common method used to estimate and remove this background from an interleaved column array has been to construct a mean per column sky value using a known region of sky background, calculating 4 sky background values for each of the amplifiers, and subtracting these single valued estimates of the sky background from each respective subimage (Hinz et al. 2006; Heinze 2007; Apai et al. 2007; Heinze et al. 2008), illustrated in Figure 1(b). This background subtraction method works well for sky background limited observations.

For exoplanet imaging surveys, the limit to the achiveable constrast close to the host star is not the sky background, but scattered light due to the atmosphere and telescope optics. In this regime, the photon flux is significantly higher than the sky background flux levels, so the simple sky background subtracton technique is not good enough and results in amplifier artifacts in the science data that reduce the sensitivity of the observations.

Residual striping in the higher flux regions near the host star contributes an additional noise component which reduces the camera's sensitivity to exoplanets when traditional PSF subtraction techniques are used - especially when the star can wander by fractions of a pixel between beamswitching operations. It becomes clear that we need a way to apply a correction that normalises the flux from each individual amplifier to a common flux reference.

3. Gradient Illumination Method for Linearising Images (GIMLI)

What is needed is a method whereby all four amplifier gain curves can be accurately related to each other, either by explicit calibration with a known photon flux source, or by a known pattern of illumination on the array. We present our algorithm for correcting the systematic effects of the four array amplifiers with our Gradient Illumination Method for Linearising Images (GIMLI).

3.1.   Taking GIMLI Calibration Data

We assume that each amplifier acts independently of one another, and that the array does not introduce time-dependent systematic effects during the array readout cycle. Read-outs are carried out with a reset-read-read cycle, which for the current Clio configuration, means that the minimum integration time for each pixel is 59.1 msec. To estimate the bias level of the camera, we take a sequence of images with the array blanked off to generate dark frames of increasing integration time, typically in steps of 50 msec up to 300 msec. The bias frame is calculated by linearly interpolating these dark frames back to an effective integration time of 0 msec.

The second image required is a frame with the array illuminated with a monotonic gradient of light varying from no illumination up to saturation on the other side of the array. To obtain this gradient of illumination, the filter wheel of the Clio camera is set to a position partway between a blanked off aperture and an open aperture. Fine adjustment of the illumination is made by rotating the wheel. Since the filter wheel is not close to a focal plane or conjugate focal plane of the array, the projected illumination gradient has no high spatial frequency components to it. The resultant image is shown in the top panel of Figure 2.

We now require two images - the Gradient Illumination Image I_{GII}, which is a full frame image corrected for the bias level, and the Smoothed GII, I_{SGII}, which is an estimate of the true distribution of light across the array. The method for obtaining the gradient image is as follows:

1. Set the Clio integration time to be as close as possible to the typical exposure time for scientific observations, typically 120-240 ms.

2. Take a set of 10 dark frames at increasing exposure times, and average these frames to produce a high signal to noise image. Construct a bias level frame by extrapolating to an effective exposure time of 0 msec.

3. In live imaging mode, rotate the filter wheel so that there is a gradient of light across the detector from the lowest flux up to saturation in a strip at the edge of the detector, about 1/5th of the width of the array. Take a set of 10 exposures and median together to increase signal to noise and to remove any transient readout effects.

To process the data and calculate the lookup table, perform these steps:

1. Subtract off bias frames from the gradient frames and average them together to form a single image.

2. To remove bad pixels, perform a 5 pixel median along each column of the image to produce I_{GII}

3. Generate the ideal smoothed image I_{SGII} by convolving each row of the image with an exponential kernel of the form $e^{-(x/\alpha)^2}$ where α is on the order of 5 pixels.

4. Split both I_{SGII} and I_{GII} into four subimages by amplifier column.

For each amplifier, plot I_{GII} versus I_{SGII} and fit a polynomial of the form:

$$I_{out} = \sum_{n=0}^{N} a_n.(I_{in})^n \tag{1}$$

using a minimization of least squares fitting technique, where N is typically 7 and a_n are the coefficients of the fit polynomial. Table 1 lists the typical coefficients for $N = 7$ order polynomial fit for Clio data. The result of plotting I_{GII} versus I_{SGII} and removing a straight line fit is shown in Figure 3. There are several points of note: there is a gap of data from 0 to 10000 DN, which represents the bias level for each amplifier. All four amplifiers show a change in gain at about 20000 DN, and other nonlinearities present up to the full well depth of 39000 DN. The higher order polynomial fit is plotted as the black line on each of the four panels. Subtracting off this higher order fit from the data is shown in Figure 4. Polynomial fits are chosen for ease of implementation and calculation, but spline fits are equally valid for use. The polynomial fits are seen to diverge from the data for 0 to 10000 DN and above 40000 DN, but this is not a problem as most data is taken with (bias subtracted) sky fluxes around 30000 DN.

3.2. Applying GIMLI Correction

For a given input image, a bias image is calculated (from Section 3.1) and subtracted off, and then each pixel in the image I_{in} is replaced by the calculated value I_{out} via Equation 1. Beamswitching is then carried out and an estimate for the differential sky flux applied to the whole image. Given the large number of images taken during thermal infrared observations, we find it more practical to generate a "lookup table" of the 65536 possible values for each amplifier and use that in GIMLI correction. This is considerably faster than calculating the polynomial coefficients for each pixel.

3.3. Limitations to GIMLI

The result of applying GIMLI to the slope image is shown in panel (c) of Figure 1. For flux levels below 30000 DN, the image is dominated by random noise. For higher fluxes, a series of systematic patterns begins to appear in the array - notably, irregularly spaced columns show higher and lower levels of signal compared to the surrounding mean, and horizontal noise bars with a pitch of 32 pixels is visible in the images.

These systematic features cannot be removed through this algorithm, as they vary as a function of row position and are not correlated with a periodicity in the column direction. The algorithm, however, presents a significant improvement over simpler techniques, reducing systematic noise by at least a factor of four.

4. Conclusions

We have presented an algorithm to calibrate out the gain differences between amplifiers read out from an interleaved array. We have shown that the algorithm removes column-dominated systematic noise patterns down to a level where other systematic artifacts are beginning to present themselves. These routines are enabling accurate point spread function subtraction techniques for the detection of faint companions to bright stars in the thermal infrared.

Facilities: MMTO.

REFERENCES

Apai, D., Meyer, M. R., Hinz, P. M., Andersen, M. A., Kenworthy, M. A., Heinze, A. N., Sivanandam, S., Miller, D., & Kasper, M. 2007, in American Astronomical Society Meeting Abstracts, Vol. 211, American Astronomical Society Meeting Abstracts, 30.04

Freed, M., Hinz, P. M., Meyer, M. R., Milton, N. M., & Lloyd-Hart, M. 2004, in Ground-based Instrumentation for Astronomy. Edited by Alan F. M. Moorwood and Iye Masanori. Proceedings of the SPIE, Volume 5492, pp. 1561-1571 (2004)., ed. A. F. M. Moorwood & M. Iye, 1561–1571

Heinze, A. N. 2007, PhD thesis, The University of Arizona

Heinze, A. N., Hinz, P. M., Kenworthy, M., Miller, D., & Sivanandam, S. 2008, ApJ, 688, 583

Hinz, P., Kenworthy, M., Heinze, A., Codona, J., & Angel, R. 2007, in Advanced Maui Optical and Space Surveillance Technologies Conference

Hinz, P. M., Heinze, A. N., Sivanandam, S., Miller, D. L., Kenworthy, M. A., Brusa, G., Freed, M., & Angel, J. R. P. 2006, ApJ, 653, 1486

Kenworthy, M. A., Codona, J. L., Hinz, P. M., Angel, J. R. P., Heinze, A., & Sivanandam, S. 2007, ApJ, 660, 762

Sivanandam, S., Hinz, P. M., Heinze, A. N., Freed, M., & Breuninger, A. H. 2006, in Presented at the Society of Photo-Optical Instrumentation Engineers (SPIE) Conference, Vol. 6269, Ground-based and Airborne Instrumentation for Astronomy. Edited by McLean, Ian S.; Iye, Masanori. Proceedings of the SPIE, Volume 6269, pp. 62690U (2006).

Table 1.   Example coefficients from fit to GII and SGII images

Coefficient	A	B	C	D
a_0	+4.3242e+00	-1.7337e+01	-1.5655e+01	+6.8873e+01
a_1	+9.9340e-01	+1.0762e+00	+1.0008e+00	+9.6042e-01
a_2	+1.1407e-05	-6.9360e-06	-1.6470e-05	-6.0089e-07
a_3	-1.6770e-09	+2.4261e-10	+1.8738e-09	+1.2134e-09
a_4	+8.9943e-14	-5.8651e-15	-8.5820e-14	-9.5092e-14
a_5	-2.1468e-18	+1.3072e-19	+1.8107e-18	+2.8345e-18
a_6	+1.9052e-23	-1.5807e-24	-1.4593e-23	-2.9731e-23
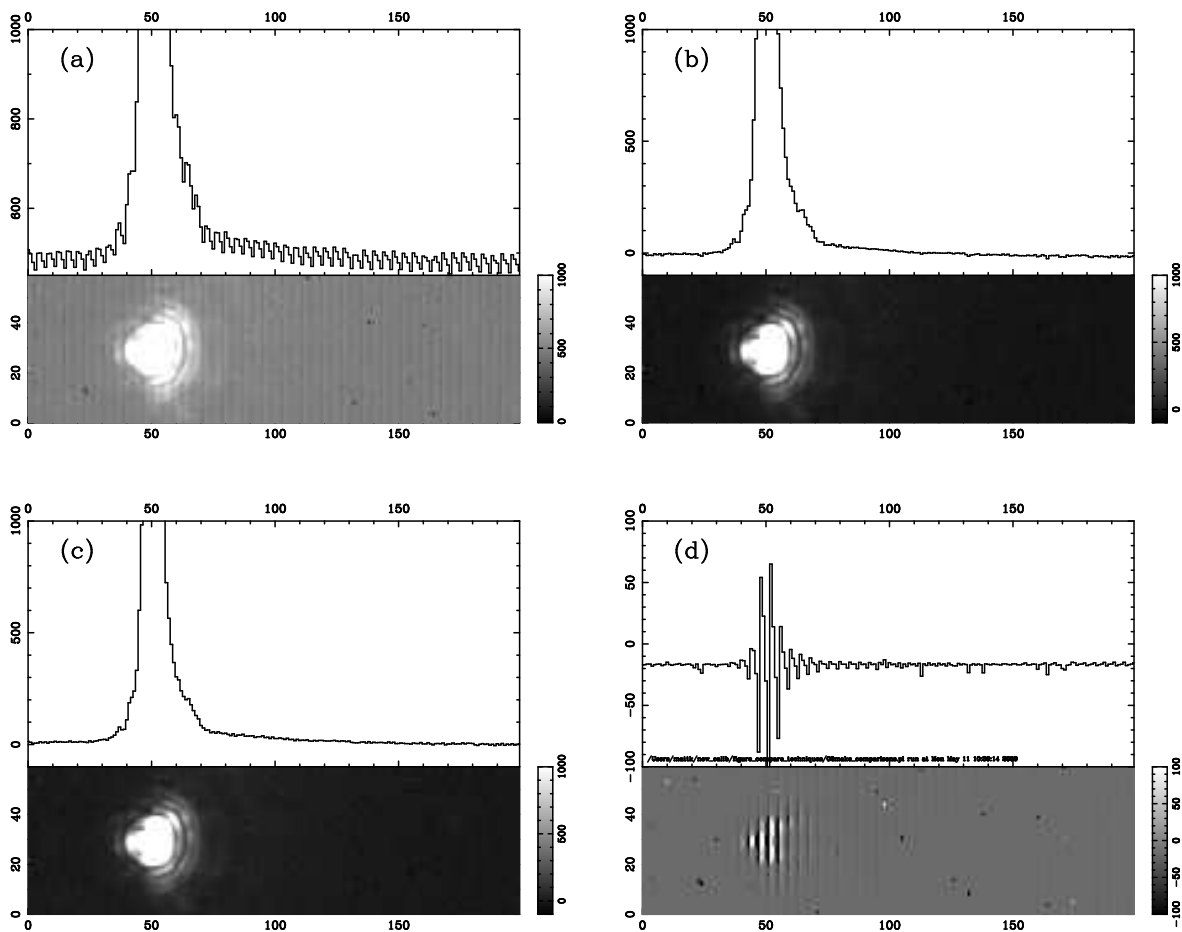
Fig. 1.— Demonstration of the amplifier gain problem for an interleaved InSb array. All four panels are observations of a bright star - the point spread function is asymmetric due to the addition of a coronagraphic optic (Kenworthy et al. 2007). Panel (a) is the result of a simple beamswitch observation. The sky background is non-zero and has the column pattern noise present. Panel (b) shows the result of estimating a mean sky background level per amplifier and subtracting this estimate off all 4 separate amplifier readouts. Panel (c) shows the beamswitched pair after passing through the GIMLI algorithm, and panel (d) is the difference image [Panel (b) - Panel (c)], emphasizing the correction applied by the GIMLI algorithm.
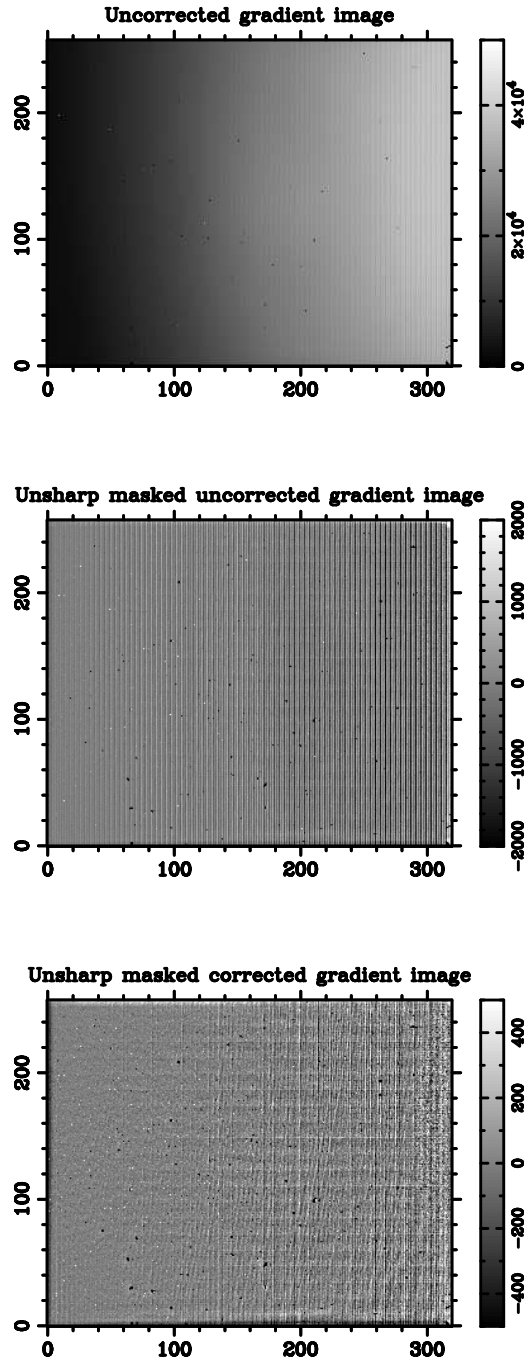
Fig. 2.— The gradient illumination image (I_{GII}) before and after algorithm correction. The top panel shows the bias subtracted I_{GII}, with the systematic column effect visible. The middle panel is an unsharp masked version of the top panel image, highlighting the column effect. The bottom panel shows the I_{GII} after applying the algorthim correction and unsharp masking.
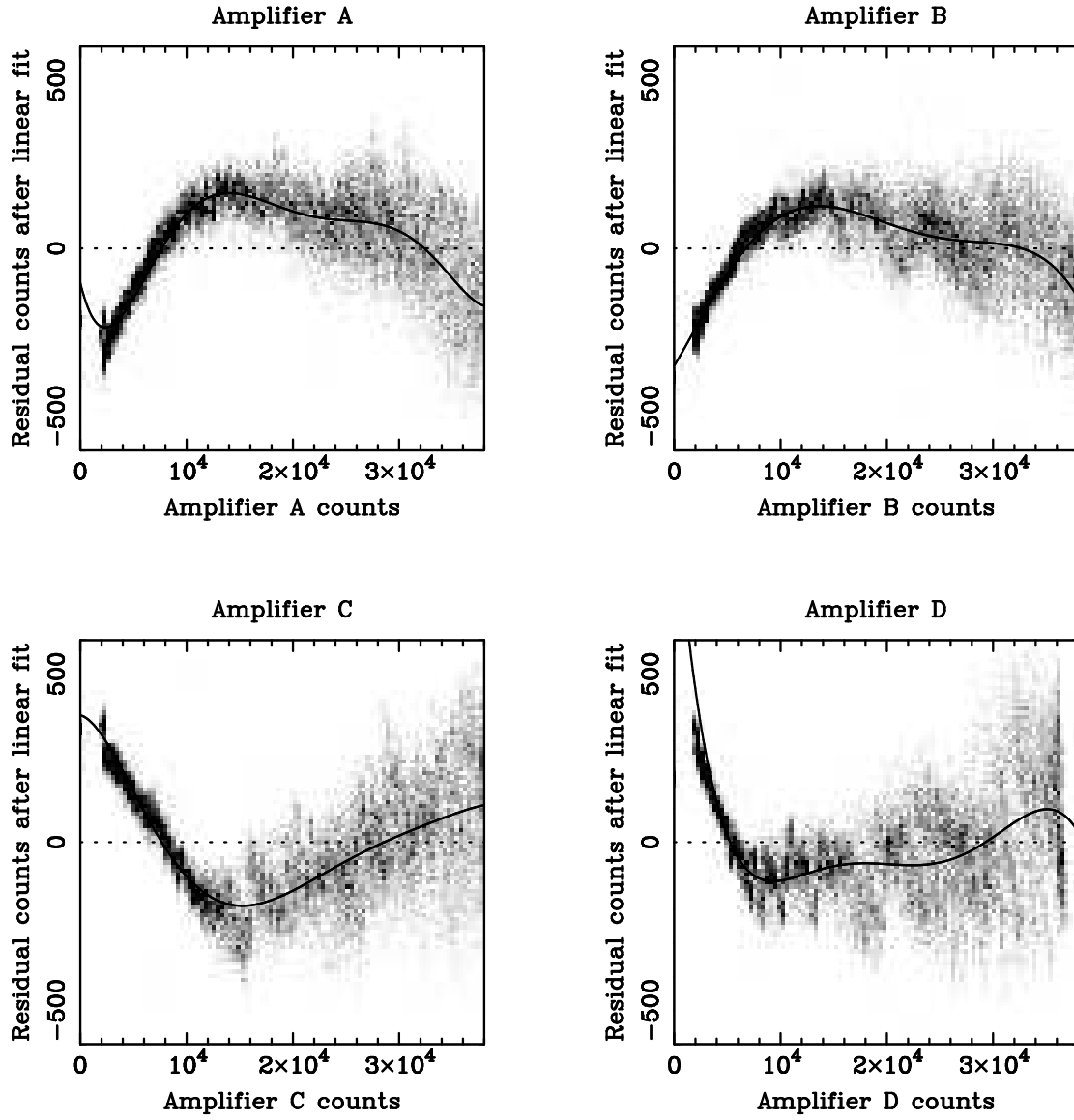
Fig. 3.— Plots of I_{GII} counts versus I_{SGII} counts after subtraction of a linear fit. Each panel represents one of the four amplifiers. The black line is a higher order polynomial fit to the data.
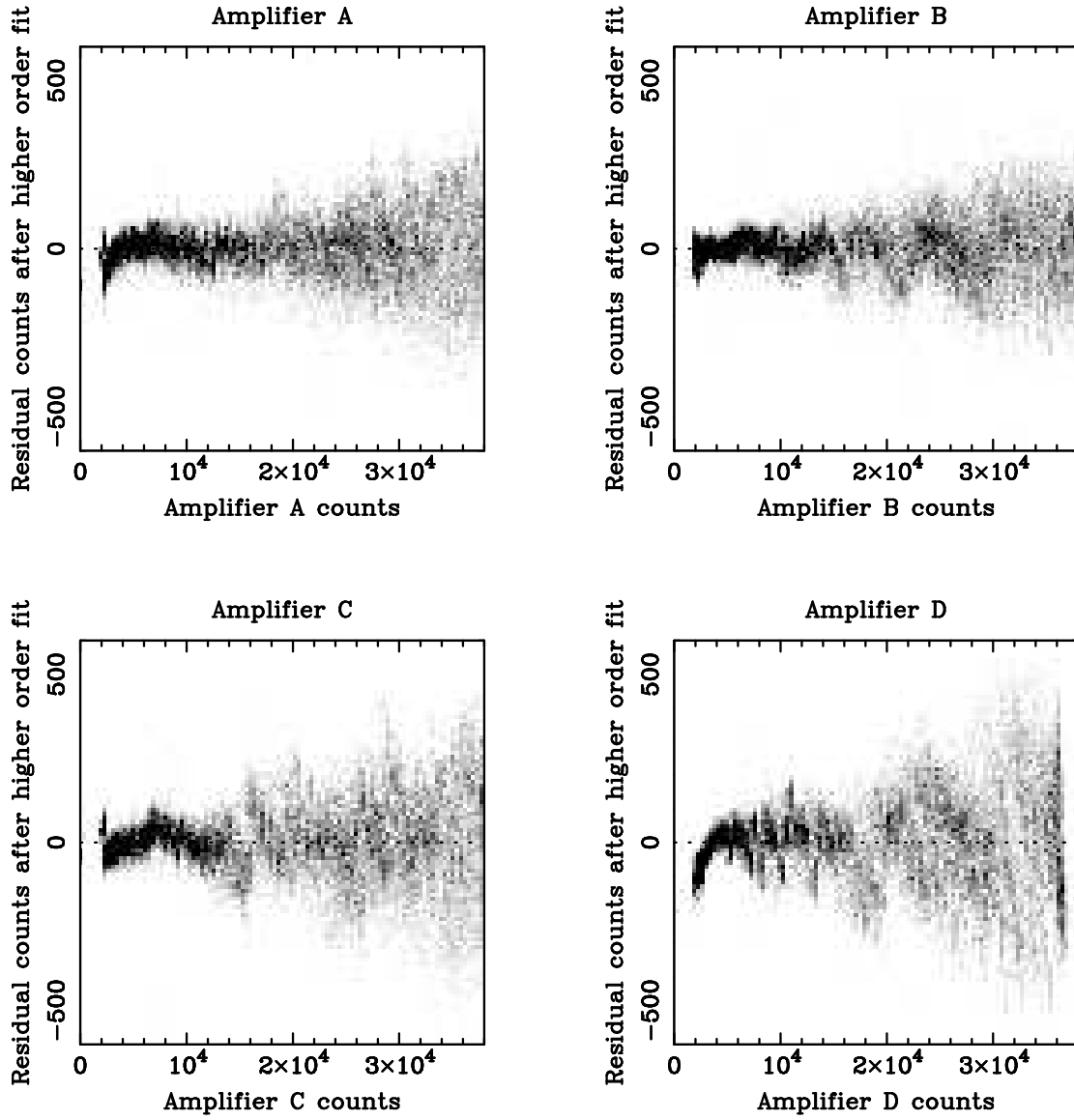
Fig. 4.— Same as Figure 3, but with the higher order polynomial fit removed.